ELSEVIER

Journal of Nuclear Materials 290–293 (2001) 295–298

journal of nuclear materials

www.elsevier.nl/locate/jnucmat

Detailed structure analysis of deposit layer in TEXTOR by means of TEM techniques

S. Muto [a,*], N. Yokoya [b], T. Tanabe [a]

[a] *Center for Integrated Research in Science and Engineering, Nagoya University, Furo-cho, Chikusa-ku, Nagoya 464-8603, Japan*
[b] *Department of Nuclear Engineering, Graduate School of Engineering, Nagoya University, Chikusa-ku, Nagoya 464-8603, Japan*

Abstract

We examined in detail the structure of the deposit layer on the main graphite belt limiter (ALT-II) in TEXTOR by means of transmission electron microscopy (TEM), electron diffraction, electron energy-loss spectroscopy (EELS) and their combination. The layer consisted mainly of an amorphous carbon matrix and a high density of crystalline boron precipitates. The amorphous carbon matrix was characterized by the stacking of pseudo-two-dimensional graphitic planes parallel to the surface of the limiter block, containing a considerable amount of boron solved. This character of deposit seems very similar to B-doped graphite irradiated by H^+.

Keywords: TEXTOR; Graphite belt limiter; Deposit layer; Transmission electron microscopy; Electron energy loss spectroscopy; Electron diffraction

1. Introduction

Hydrogen (tritium) retention in deposited layer and its removal are key safety issues for construction of a D-T burning machine. Hydrogen is occluded in co- or re-deposited layer as a result of plasma and materials interactions, erosion, ionization, transport, charge-exchange, and deposition [1–4]. The structure of the deposit, therefore, results from very complex hydrogen effects. Ion beam techniques are very useful to determine how much hydrogen is retained and what kind of elements are included. However, they are powerless to determine the structure of the deposit. Without the knowledge of chemical nature and crystalline structure, it is difficult to design how to remove the tritium from the deposit.

We present in this report the results of detailed structural analysis of the deposit on main graphite belt limiter (ALT-II) in TEXTOR by means of transmission electron microscopy (TEM) techniques. The TEM techniques applied here, include conventional TEM, high-resolution TEM (HRTEM), electron diffraction (ED) and electron energy loss spectroscopy (EELS), which enable us to make structure and chemical analyses.

2. Experimental

In Fig. 1(a) is shown the internal structure of TEXTOR. The deposit layer which is examined here is from the #22 graphite limiter block as shown in Fig. 1(b). The deposit layer was removed from the framed area with adhesive tape. The removed layer was repeatedly cleaved and one of the fragmented pieces was then pasted on a single-hole copper disc, followed by argon ion-milling until the sample was perforated. It followed that the sample surface was roughly parallel to the surface of the limiter block.

The sample thus prepared was examined with a Jeol-JEM200CX transmission electron microscope (operated at 160 kV) equipped with a parallel electron energy-loss spectrometer (PEELS), Gatan DigiPEELS model 766. High-resolution imaging was also conducted with a Hitachi H-1250ST high voltage electron microscope (HVEM), operated at 1 MV.

* Corresponding author. Tel.: +81-52 789 5157; fax: +81-52 789 3791.
E-mail addresses: muto@cirse.nagoya-u.ac.jp (S. Muto), tanabe@cirse.nagoya-u.ac.jp (T. Tanabe).

0022-3115/01/$ - see front matter
PII: S0022-3115(00)00576-6

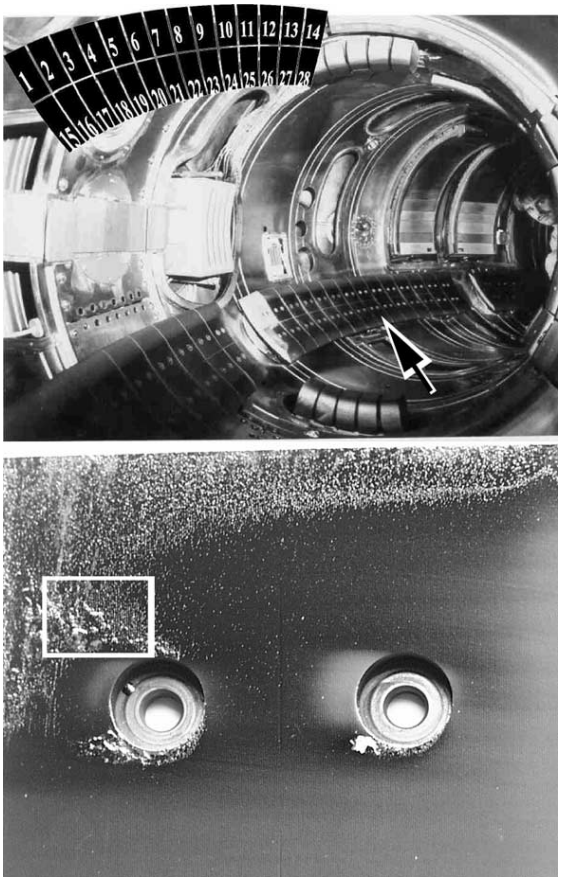

Fig. 1. (a) Inside view of TEXTOR fusion device. The position of #22 limiter block is indicated by an arrow. (b) A portion of #22 graphite limiter block. The framed area of the deposit layer was removed by adhesive tape for the TEM sample.

3. Results

3.1. TEM characterization

Bright and dark field TEM pictures of the deposit layer, together with the ED pattern are shown in Figs. 2(a)–(c), respectively. The dark dots of precipitates in the bright field image appear bright in the dark filed image taken from the encircled portion of the Debye–Scherrer rings. The ED patterns from the deposit are basically superposition of the sharp Debye–Scherrer rings and the diffuse halo pattern, though the latter is not clearly seen in Fig. 2(c) because it was taken from the area of a high density of precipitates. The image is hence, simply understood by a mixture of an amorphous-like matrix and crystalline precipitates, 3–50 nm in size, appearing as dark contrast in the bright-field image (a). The amorphous matrix is graphitic amorphous carbon-like because the radius of the first halo ring is consistent with the amorphous graphite formed

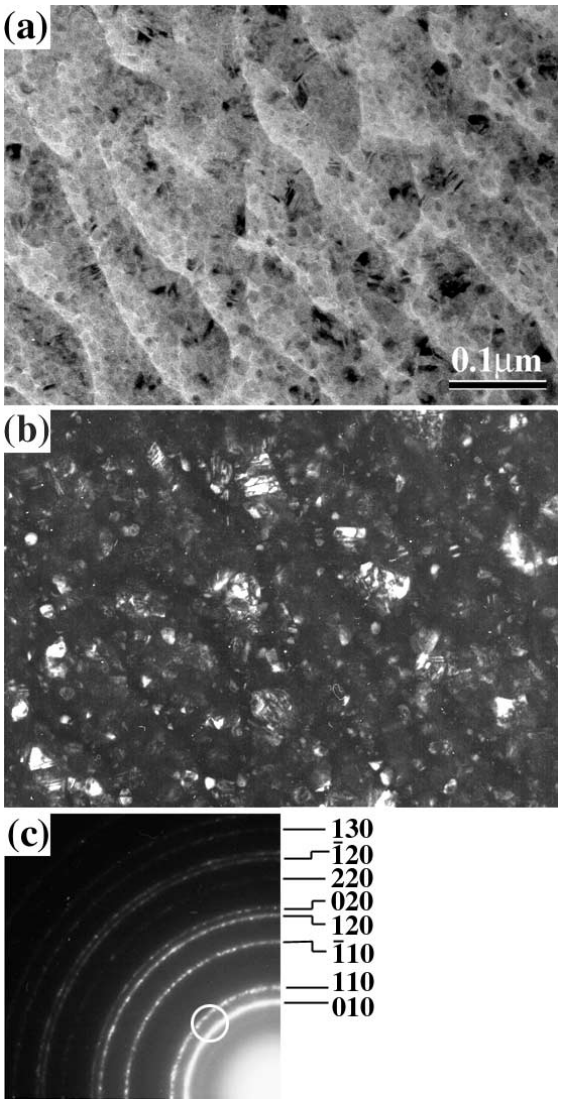

Fig. 2. (a) Bright-field TEM image of the deposit layer. (b) Dark-field image taken from the encircled portion of the diffraction pattern (c). (c) Electron diffraction pattern indexed by the crystalline boron structure. See text for detail.

by electron or ion irradiation onto crystalline graphite, rather than diamond-like tetrahedral amorphous carbon. It should be noted here that the HRTEM observation along the sample surface normal exhibited no lattice fringes corresponding to the graphitic basal planes. This suggests that the amorphous matrix may show structural anisotropy unlike general amorphous structures. This point will be discussed later.

To identify the precipitates, we examined all possible structures available in the Pearson's Handbook of Crystallographic Data [5]. According to the phase diagram of the B–C system, the possible phases are graphite, B_4C and B. We found that only crystalline

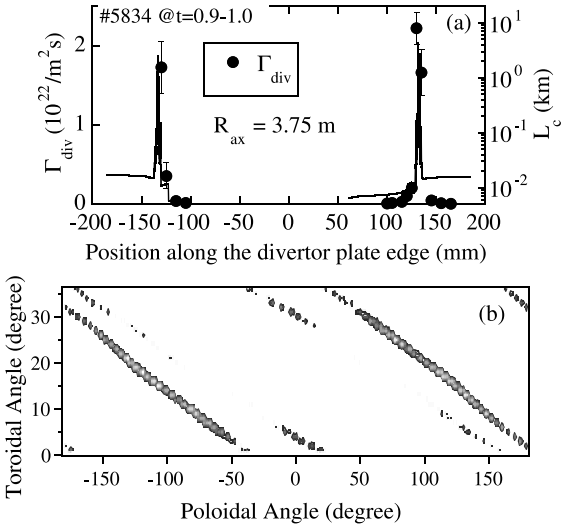

Fig. 3. Electron energy-loss raw spectrum from the deposit layer in 100–600 eV.

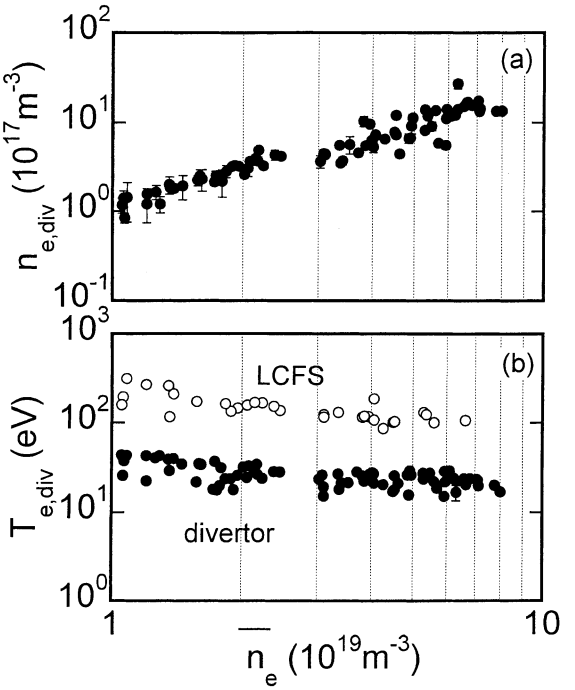

Fig. 4. Comparison of EEL spectra in 150–350 eV from the deposit layer, crystalline boron and B_4C from top to bottom. The pre-edge backgrounds are subtracted.

boron (Pearson Symbol: hR12, space group 166: R $\bar{3}$m, $a = 0.506$ nm, $\alpha = 58.06°$) was consistent with the ED pattern among all crystal structures consisting of carbon and/or boron, as indexed on the right side of (c).

3.2. EELS measurement

In TEXTOR, boronization is routinely employed and occasionally siliconization is utilized. Accordingly, C and B are the main components of the deposit with a detectable amount of O and Si. An EELS spectrum over the energy-loss range of 100–600 eV is shown in Fig. 3. It is seen that the deposit layer comprised considerable amount of boron, carbon and a small amount of oxygen, but silicon was not detected within the present detection limit (<1 at.%). The quantitative elemental analysis resulted in the composition ratio (atomic), B:C:O = 1.0:0.7:0.3 within the uncertainties of ±10%.

EELS core-loss spectra are compared for the present sample, a B_4C and pure boron crystal in Fig. 4. The corrections were made by the Fourier-ratio deconvolution to obtain the single loss spectra. The energy-loss near edge structure (ELNES) of the boron K-absorption edges generally reflect the atomic configuration and bonding information near the excited atom. The ELNES of boron edge from the sample of interest cannot be explained only by crystalline boron because in (a) the first main peak at 191 eV has a small shoulder at 189 eV, and the first minimum and the second maximum were blunt and blurred, compared to (c), partly because the structure is amorphous. It seems plausible to interpret that the spectrum (a) is a weighted sum of the spectrum (b) and (c) around the onset of the absorption edge. Remembering that the Debye rings in the ED (Fig. 1(c)) showed no indication of crystalline B_4C, the B-ELNES could be best interpreted by a mixture of pure B crystallites and boron–carbon composite presumably in a form of substitution of boron atoms on threefold coordinated sp^2-sites within the graphite network.

The feature of C-ELNES supports the above interpretation (Fig. 4). The C-ELNES in (a) has blunt profile, consistent with the amorphous structure, and π^* peak ($1s \rightarrow 2p\pi$-antibonding state). The structure of amorphous matrix is thus graphitic carbon with the sp^2 hybridization. Note that the π^* peak is shifted to the lower energy side by a few eV compared to that of crystalline and amorphous graphite. This indicates the presence of considerable amount of B–C bonding, which is of the binding energy less than C–C bonding, consistent with the lower melting point of B_4C compared to graphite.

The sp^2 hybrid orbitals have uniaxial anisotropy so that the wavefunction of the π-antibonding state extends predominantly perpendicular to the basal plane unlike the σ-state. The transition from 1s to 2p-π^* is only allowed when the momentum transfer has a component parallel to the anisotropy axis [6]. To examine the structural anisotropy of amorphous matrix, the C–K edge spectra were acquired from the transmitted beam only at the diffraction mode with the collecting semi-angle of 0.6 miliradian, making an angle θ of 0, 10 and 20 degrees between the sample surface normal and the in-

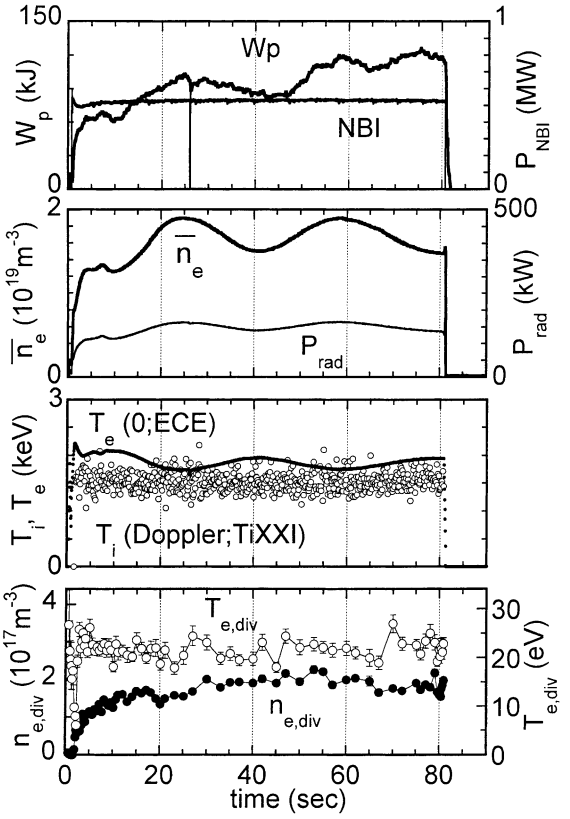

Fig. 5. Change in the intensity ratio of π^* and σ^* core-loss spectra as a function of the angle, θ, between the sample surface normal and incident electron direction (solid circle). The broken line illustrates $\cos\theta$.

cident electron beam. In this instrumental configuration, the EELS detector collects the momentum transfer of electrons mainly in the direction of incident electrons (zero scattering angle). As a result the intensity ratio of π^* and σ^* peak was slightly but systematically decreased with the beam inclination angle, as shown in Fig. 5. The data was normalized by the peak ratio at $\theta = 0°$ and the correction of multiple scattering was made. The angular dependence deviates from the expected $\cos\theta$-dependence, presumably because of the incident beam convergence. This result suggests that the local long axis of the π-antibonding wavefunction is oriented predominantly normal to the sample surface and, therefore, the amorphous matrix has likely the parallel turbostratic layer ordering of fine granular hexagonal networks.

4. Discussion and summary

The origin of the crystalline B precipitates could be mostly boronization because carbon atoms in the 6-member atomic rings are chemically inactive and the deposited B during the boronization cannot bind to C atoms. On the other hand a considerable amount of solute B is likely produced by co-deposition during plasma shots because the B- and C-ELNES profiles presented here are very similar to those of a carbon–boron alloy prepared by chemical vapor deposition (CVD) at ~1000°C with high boron doping levels, typically 25 at.%, reported by Serin et al. [7]. Their results clearly demonstrated the presence of boron substitution simply within an sp^2-bonded graphite network for the CVD process at high temperature, and similarly in the present case the high solubility limit for boron in graphite due to PMI suppresses B_4C precipitation.

The amorphous part should include both sp^2 and sp^3 bonded carbon atoms, which is a characteristic of amorphous carbon. This is not only because the deposition occurred by shot-by-shot but also the deposit includes about 10–20% deuterium [4], which makes sp^3-bonding with carbon atoms. Since the present TEM techniques cannot see hydrogen, we could not tell at present whether deuterium is dissolved in the B crystallites.

In summary, the deposit layer consisted mainly of an amorphous carbon matrix and a high density of crystalline boron precipitates. The amorphous matrix was characterized by the stacking of pseudo-two-dimensional turbostratic layers parallel to the surface of the limiter block, containing a considerable amount of boron in a form of substitution on threefold coordinated sp^2-sites within the graphite network. All these results make us to conclude that the character of the deposit seems very similar to B-doped graphite irradiated by hydrogen ion.

It should be mentioned that the present analysis is limited to a small part of the deposit layer in a particular limiter block. The deposit layer in a tokamak is expected to be inhomogeneous and we have taken samples from several other blocks. Their analysis is now in progress and the results will be reported elsewhere.

References

[1] G. Mank, V. Philipps, H.G. Esser, W. Biel, M. Brix, K.H. Finken, A. Pospieszczyk, Physica Scripta T81 (1999) 70.
[2] M. Rubel, V. Philipps, A. Huber, T. Tanabe, Physica Scripta T81 (1999) 61.
[3] A. Pospieszczyk, V. Philipps, A. Huber, A. Kirschner, B. Schweer, E. Vietzke, Physica Scripta T81 (1999) 48.
[4] K. Ohya, T. Tanabe, M. Wada, T. Ohgo, V. Philipps, B. Unterberg, A. Pospieszczyk, B. Schweer, A. Huber, N. Noda, Nucl. Instrum. Meth. Phys. Res. B. 153 (1999) 354.
[5] P. Villars, L.D. Calvert, Pearson's Handbook of Crystallographic Data for Intermetallic Phases, vol. 1 ASM, 1985.
[6] R.A. Rosenberg, P.J. Love, V. Rehn, Phys. Rev. B 33 (1986) 4034.
[7] V. Serin, R. Brydson, A. Scott, Y. Kihn, O. Abidate, B. Maquin, A. Derre, Carbon 38 (2000) 547.